IJREB

ISSN **2321-743X**

International Journal of Research in

Engineering and Bioscience

Volume **7** Issue **1** (Pages 1- 13)

Journal home page: www.ijreb.org

EFFECT OF pH ON $BaZrO_3$ PEROVSKITE NANOPARTICLES VIA SOL-GEL AUTO-COMBUSTION METHOD

[1, 2] J. Abimalar and [1, 2] V. Anslin Ferby

[1]Department of Physics and Research Centre,
Scott Christian College (Autonomous), Nagercoil - 629 003, Tamil Nadu, India
[2]Manonmaniam Sundaranar University,
Abishekapatti, Tirunelveli - 627 012, Tamil Nadu, India

Corresponding author: jabimalar98@gmail.com

ABSTRACT

The sol-gel auto-combustion technique was used to synthesize barium zirconate ($BaZrO_3$) nanoparticles and maintaining a fuel to oxidant (F/O) ratio at 1.The synthesized samples have been characterized by X-Ray Diffraction (XRD), Fourier Transform Infrared (FTIR), Ultraviolet Visible spectroscopy (UV-Vis), Photo Luminescent (PL) and Scanning Electron Microscope (SEM) and the effect of pH on the structural, morphological, and optical and emission properties of the samples were studied. XRD pattern confirmed that the prepared samples were crystalline. The crystallite size of the Barium Zirconate synthesized powder decreased with an increase in pH value. The crystallite size of the sample was found to be 48.03 nm, 35.84 nm and 34.82 nm for the pH values 5, 7 and 9 respectively. The phase purity of $BaZrO_3$ nanopowders has been examined by Fourier transform infrared spectroscopy (FTIR). The observed band at 1445 cm^{-1} confirmed the Ba–O stretching vibration. The bands at 849, 549 cm^{-1} confirmed Zr-O vibrations. UV-Vis absorption and photoluminescence (PL) measurements were used to explore a variety of optical characteristics. The tauc plot is useful in order to estimate a semiconductor material's energy gap from its absorption spectra. Tauc plot exhibited the variation of band gap from 4.86 eV to 4.95 eV. Green and red occur as the main emission bands in the PL spectra of the synthesized phosphor in response to an excitation wavelength of 230 nm. SEM images of prepared samples have irregularly shaped large grains with visible particle sizes.

Keywords: Nanoparticle; Combustion synthesis; X-ray diffraction; FTIR; UV-Vis absorption; photoluminescence; SEM

INTRODUCTION

1. Introduction

BaZrO3 has developed in significance in the area of electronic ceramics [1] because to its good mechanical strength [2], high heat stabilization [3], small thermal expansion coefficient [4], high melting point (2600 °C) [5,6] and great chemical stability [7]. Due to these characteristics, BaZrO3 has drawn attention for a wide range of applications, including crucible material in processes involving the highly corrosive oxide melt [5], moisture sensor [8], electrolyte in fuel cell devices [9], thermal barrier coating in the aircraft industry [10], and a number of other uses.

For the sol-gel auto-combustion synthesized method to produce $BaZrO_3$ nanoparticles, the fuel to oxidant ratio required to be carefully adjusted at 1. The sol-gel auto-combustion synthesis method produces grains with an average size of 39 nm that were then sintered at 1200 °C for two hours to generate particles with high density [5,11]. In an effort to lower the high heating temperature to around 1200°C, small amounts of metallic elements such Co, Zn, Ni, and Cu were employed as a sintered promoting agent that improve in sinterability [12 -15]. The highest density was only 99% when sintering aids were employed [14]. Due of the rigorous requirements of stoichiometry control, high sintering temperatures, and the usage of sintering aids, it is crucial to discover an alternate method of making BaZrO3 crucibles. To make highly dense BaZrO3 material, the process parameters must be enhanced. Combustion-based methods that result in homogeneous molecular mixing of the precursors are known to lower comparative chemical diffusion length and final synthesis temperature [16, 17]. Solution combustion synthesis, where the initial reactive component is in an aqueous solution known as a sol-gel, is a common method that has shown to be easy to use, cheap to utilize, and power - efficient [21–23, 25–27, 28, 29]. Solution synthesis is favored over sol-gel auto-combustion synthesis for producing nano-sized, uniform, and phase-pure ceramics due to the fine particle size and boundaries of particle size of the obtained powders [18], the easy to control stoichiometry, the high crystallinity, and the total control of particle morphology [20–23, 25–27, 28, 29]. According to this method, a locally produced anionic redox reaction occurs under the influence of heat, and the resultant combustion wave subsequently spreads throughout the rest of the sample [17, 21, 24]. As the exothermic reaction between the oxidant and the reductant can produce energy levels high enough to enable the process self-propagating, an external source is no longer required to initiate the reaction [24]. A sol-gel is generated in the citrate-nitrate sol-gel auto-combustion method by combining metal nitrates, which serve as oxidizers, with citric acid, which serves as a fuel and a chelating agent [30]. These elements come together to create stable, crystalline metal-citrate

complexes, often known as gels [18, 19]. The pH of the solution, which controls the concentration of H^+ ions in the sol and determines how the metal-oxygen linkages in the gel are polymerized, has a big impact on the citric acid's capacity to operate as a chelating agent. Because of this, the pH of the solution used to form the gel has a big impact on how uniform the gel is since it impacts how the metal ions interact with the citric acid. Reduced porosity allows for ceramics to be sintered at very high densities since the final ceramic is evenly distributed throughout without agglomerating at various spots when the uniform gel combusts [31–33].

In studies that use pH variations of the sol, calculations on the role of pH on the sols or possible intermediary species that may occur during the gelation process are often not presented. We study the effects of these parameters on the phase purity of the gel and their relationships to the resulting $BaZrO_3$ ceramic grain sizes in order to fabricate exceptionally dense, phase pure, uniform, and Nano sized $BaZrO_3$.

The main focus of this research is on the synthesis of $BaZrO_3$ ceramic with these characteristics. The pH was modified using a sol-gel auto-combustion method to a range of 5, 7, and 9, while the fuel to oxidant ratio was kept constant at 1.

2. EXPERIMENTAL PROCEDURE

2.1 Synthesis of $BaZrO_3$ Nanoparticles

Making sol-gels of citrates (C) and nitrates with a fixed fuel to oxidant ratio (F/O ratio) and adjusting the pH of the solution allowed developing pure, nano-sized $BaZrO_3$. The methods for creating sol-gels with various pH values are schematically described. Citric acid, $C_6H_8O_7$, was used as the fuel and $Ba(NO_3)_2$ and $ZrO(NO_3)_2$ were used as the oxidant. The estimated and optimised ideal fuel (F) to oxidant (O) ratio (F/O) was 1, and $Ba(NO_3)_2$, $ZrO(NO_3)_2.H_2O$ and citric acid was dissolved in distilled water to create a solution. NH_4OH was gradually added to maintain pH of the solution. With steady stirring using a magnetic stirrer, the pH-adjusted solution was then heated to 80°C to produce a viscous gel. This study concentrates on the features of three distinct solutions with pH values of 5, 7, and 9. After that, this gel was vacuum dried at 100°C for 4 hours to start the auto-combustion reaction. After this combustion producing ash that was uniformly fluffy and grey in texture.

2.2 Characterization

A Bruker EVA 6.0, MTC high temperature chamber, RT to 1600°C, Cu anode with 3kW generator, twin-twin optic (motorized slit and goebel mirror), and a LYNXEYE Family detector were used to characterize the samples (0D and 1D mode). The patterns were scanned in the 2θ range 25 to 75; at a maximum angular speed of 20 s. The functional groups in the generated powder and the particles that were calcined at different temperature were detected

using FTIR (Spectrum BX Spectrometer). For this, 1% of the material was mixed and crushed with 99% KBr. The powder mixture was compressed into 10 mm - diameter tablets for FTIR measurements with a force of 5 tonnes for 2 minutes. The spectra were collected with resolution 4 and 128 repeats scanning in the 400 – 4000 cm^{-1} range. Using an HITACHI S2600N - model scanning electron microscope (SEM), running at 25kV in vacuum, the samples' structure and morphology were examined. Powder samples were used for the SEM examinations. The electron microscope had an energy dispersive X-ray connection (EDAX/2001 equipment) for the elemental analysis. Studies on UV-Vis were carried out using a thermal fishing assessment 220 UV-DRS-Spectrometer with a 190–1100 nm wavelength range. Oxford Low Temperature LN2 77k Setup and High Temperature 100 373k Set Up were used to capture photoluminescence spectra from the Varian Cary Elipse Photo Luminescence Spectrometer.

3. Results and discussion

3.1. X-ray diffraction analysis

Fig. 1 shows the X-ray diffraction pattern of Barium Zirconate nanostructures as a function of increasing pH (from 5, 7& 9).

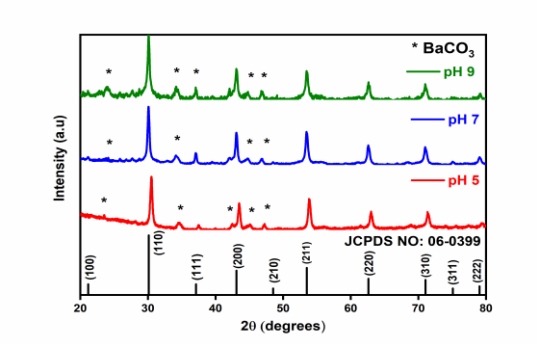

Fig. 1 XRD patterns of the $BaZrO_3$ samples for different pH

All the diffraction peaks in the pattern well matched with the available Joint Committee on Powder Diffraction Standards for $BaZrO_3$ (JCPDS 06-0399) and are indexed as the cubic Barium Zirconate with lattice constants a = 4.193 Å. $BaZrO_3$ peaks in the spectrum with higher intensities and smaller spectral widths clearly showed the strong crystallinity of the final products. Very small amount of $BaCO_3$ (*) compound presented. The dissolution of carbon dioxide (CO_2) from the air in the water leads to the formation of $BaCO_3$. When results from alternative methods for elimi nating the secondary phases of barium car bonate are compared to those obtained using thi s method without treatment, good phase purity i s found [34, 35, 36].

In the (110) diffraction plane, which appears to indicate the dominant peak on the highest crystalline sample, XRD peak profile analysis was carried out for all samples (Fig. 1) The interplanar spacing d was calculated [37] using Eq. (1).

$$n\lambda = 2d\sin\theta \quad (1)$$

Where λ is the X-ray wavelength, n = 1 for the first diffraction order and θ is the peak position.

The estimated d was found to be smaller than the standard value (2.965 Å). Using Eq (2), the crystallite size D was determined from the (110) plane [38].

$$D = 0.9\lambda / ((\pi\beta/180)\cos\theta) \quad (2)$$

Where "β" is the full width at half maximum (FWHM) of the 110 diffraction line, the value of D decreases like 48, 35 and 34 with increasing pH value 5, 7 and 9 respectively.

Table 1: Calculated lattice parameters of $BaZrO_3$ nanoparticles

Parameters/ Sample	pH 5	pH 7	pH 9	Standard
Lattice constant (Å)	4.14	4.20	4.19	4.19
Unit cell volume V(Å)^3	71.12	74.56	73.91	73.72
Crystallite size D (nm)	48.03	35.84	34.81	-
Density (ρ) g/cm^3	6.45	6.16	6.21	6.22
Dislocation Density(×10^{14}) Lines/metre	4.33	7.78	8.24	-
Surface area (S)×10^{6}cm^2/g	0.19	0.27	0.28	-
Micro strain (ε) x 10^{-3}	0.00019	0.00025	0.00025	-

3.2. FTIR analysis

Fig. 2 shows the FTIR spectra of the gel formed at 100°C by centrifuging the solution after a 4 h reaction period, and calcined at 1200°C for 2 hours. Here is the infrared spectrum of pure barium zirconate for reference. The existence of water and hydroxyl groups adsorbed on to gel particles leads to a big peak to occur at almost 3417 cm^{-1}. Tiny peaks in each sample, 2450 and 2363 cm^{-1}, have been connected to atmospheric carbon dioxide. The C=C groups and C=O groups were generated by carboxylic acid, and their respective highest bands were detected at 1,640 cm^{-1} and 1,750 cm^{-1}, respectively. Pure $BaZrO_3$ is assumed to be the cause of the gel's broad vibration band at 1445 cm^{-1} and other, sharper vibration bands at 849 cm^{-1}. The broad vibration band seen in the synthesized $BaZrO_3$ nanopowder at a wavelength of 549 cm^{-1} is a result of the Zr-O vibration of the perovskite structure.

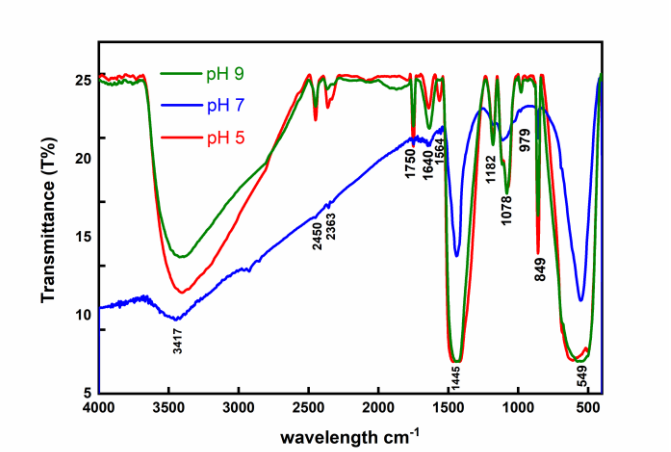

Fig.2 FTIR spectra of $BaZrO_3$ nanopowder samples Prepared for different pH

3.3. SEM analysis

SEM photomicrographs of pure barium zirconate powders that were produced after heated to 1200°C for two hours are shown in Fig.

3. The temperatures of the combustion synthesis process generally cause the particle formation to agglomerate and become coarser. All morphologies evaluated by the SEM had pH values that showed no detectable variation. It is observed that the generated powders have the morphology of agglomerates with no clear shape, and the particles attach to one another and create a network-like structure as has been shown. Moreover, laser diffusion was utilized in order to identify the distribution of particle sizes of the powder that was calcined at 1200°C. The particle aggregation that takes place at high temperatures is explained by the non-uniform particle distribution in the synthesized perovskite. [39].

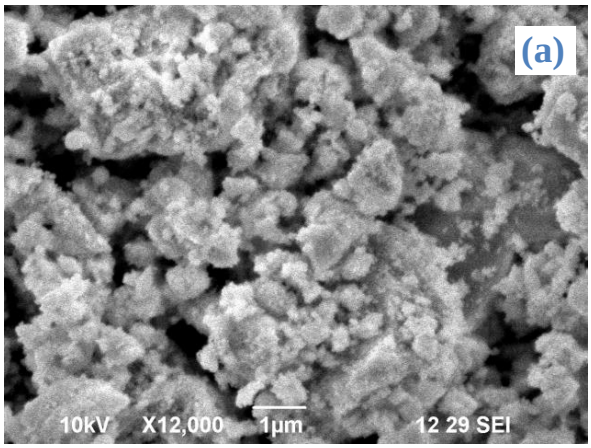

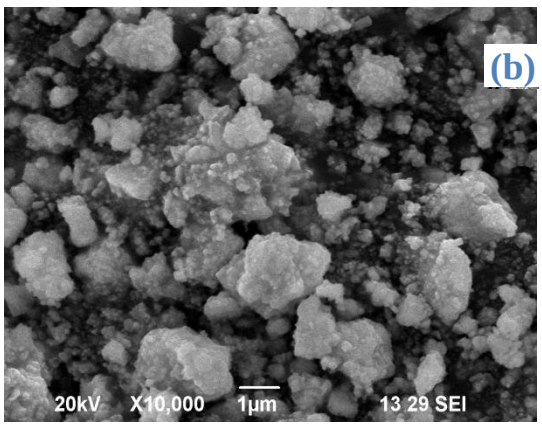

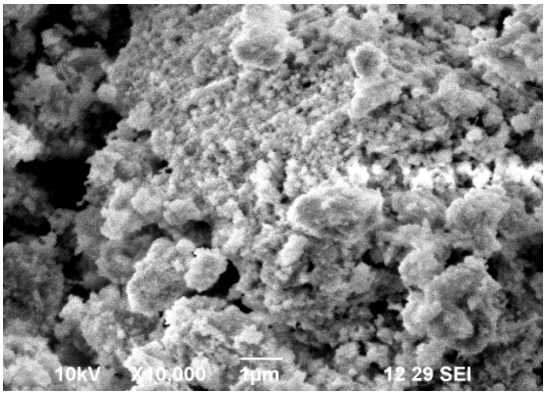

Fig.3. SEM micrographs of $BaZrO_3$ samples prepared for different pH.

3.4. Elemental Analysis – EDAX

Fig. 4 displays the energy dispersive absorption X-ray spectra of $BaZrO_3$ samples obtained for different pH (5, 7 & 9).It can be seen that every peak is attributed to the native constituents of the compound BaZrO3: Barium (Ba), Zirconium (Zr), and Oxygen (O). The absence of any extra peaks that could be ascribed to contaminants is evidence of the synthesized $BaZrO_3$ samples purity.

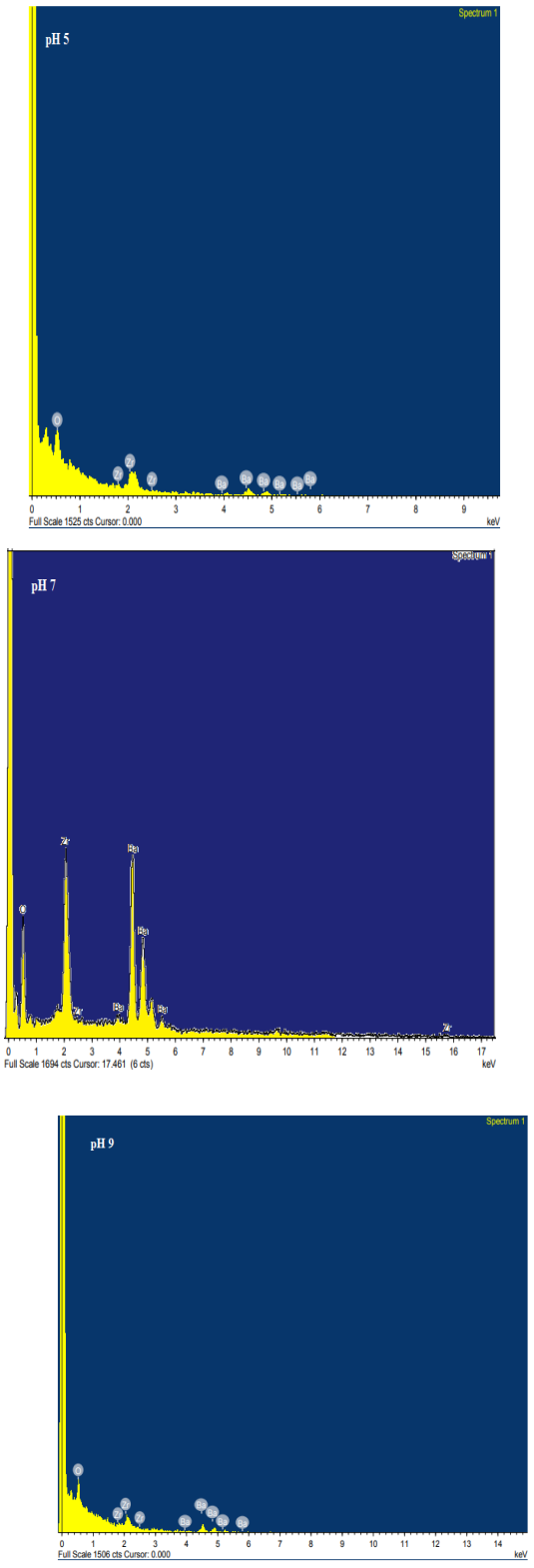

Fig.4 EDAX spectra of $BaZrO_3$ samples prepared for different pH

The related quantitative elemental analysis is summarised in Table 2. For all three samples, the atomic percentages of the three elements are approximately stoichiometric to the BaZrO3 compound.

Table 2 Elemental composition of $BaZrO_3$ nanopowders

Samples with different pH	Elements in mass percentage			Elements in atomic percentage		
	Ba	Zr	O	Ba	Zr	O
pH 5	0.36	0.39	1.33	2.95	4.75	92.30
pH 7	49.63	24.63	25.74	16.13	12.05	71.82
pH 9	0.47	0.28	1.13	4.47	4.02	91.51

3.5. UV Absorption Studies

The UV-Vis absorbance spectrum of $BaZrO_3$ ceramics is shown in fig. 5. The peak around 230 nm can be attributed to band edge absorption of $BaZrO_3$.

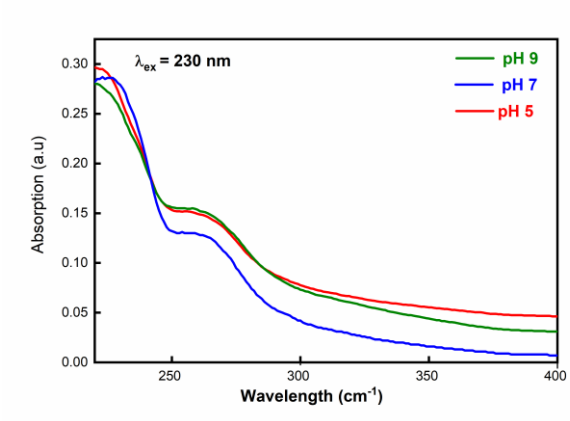

Fig. 5 UV-Vis absorbance spectra of $BaZrO_3$ samples prepared for different pH

The energy needed to excite an electron from the valance band to the conduction band is known as the band gap energy of a semiconductor. In order to accurately anticipate the photo-physical and photocatalytic properties

of semiconductors, the band gap energy must be determined. The following equation was used to estimate the photonic band gap energy (E_{gap}):

$$(\alpha h\nu)\ \alpha\ (h\nu - E_{gap})^{n} \qquad (3)$$

where h is the Planck constant, ν is the frequency of the photon, E_g is the energy of the band gap, and the "n" factor depends upon the type of electron transition and is equal to either 1/2 or 2 for the direct and indirect transition band gaps, respectively [40]. A straight line is simply fitted to the linear portion of the absorption spectra in the "direct extrapolation" (DE) Tauc method for determining band gaps [41]. This method proposed by Wood and Tauc [42] .

Fig. 6 shows the Tauc's plot of $BaZrO_3$ for pH 5,7 and 9. For the various pH levels, it is found that the band gap of pure $BaZrO_3$ at room temperature is 4.86, 4.90, and 4.95 eV. As pH increases, the bandgap values decrease. The decreasing Egap values may be caused by oxygen vacancies, lattice defects, and/or local bond distortion in order to form discrete electronic levels in the material's band gap. [43]. Due to its wide optical band gap, the synthesized $BaZrO_3$ material looks promising as a UV detecting device.

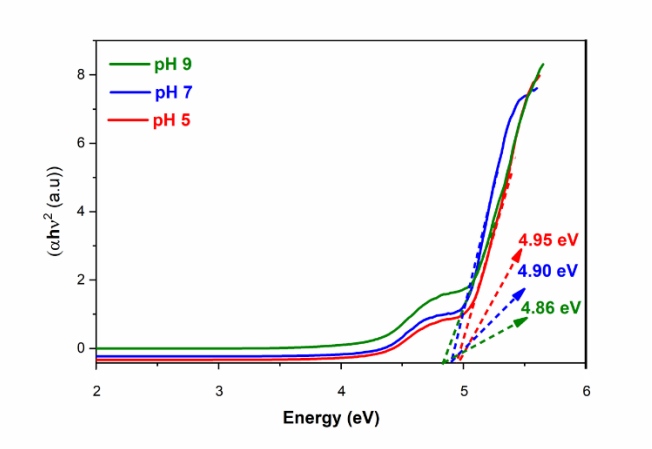

Fig.6 Tauc plot of $BaZrO_3$ samples prepared for different pH

3.6. Photoluminescence Study

An effective method for analyzing the degrees of structure and function at medium range is PL spectroscopy [44]. The PL technique's extreme sensitivity frequently reveals characteristics that UV-Vis absorption measurements hardly ever characterize. For identifying a class of energy levels that cannot be observed by UV-Vis measurements of absorption, PL is a very useful technique [45, 46].

Fig.7 illustrates the photoluminescence spectra of $BaZrO_3$ samples generated for three different pH values (with 230 nm excitation) at room temperature.

The PL emission of pure $BaZrO_3$ consists of two main parts: one is in the ultraviolet (UV) region at 230 to 260 nm while the other is in the visible light (VL) region; the strongest emission band located at 500 nm with 2.48 eV is a typical

green band. And another emission band located at 750 nm with 1.65 eV is a red band.

Even though to their many uses in solar-blind photo detection, security, sterilization, and other fields, solid-state deep ultraviolet (DUV) optoelectronic devices in the ultraviolet-C (UVC) spectral range have received an abundance of research. [47 – 53].

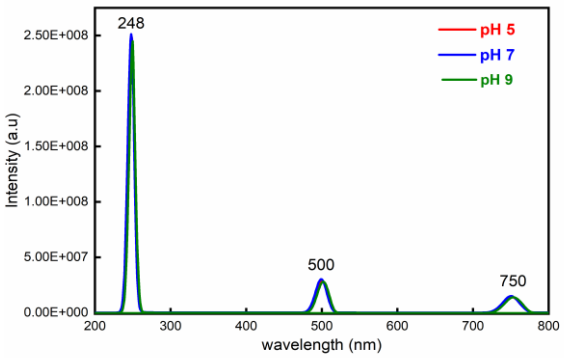

Fig. 7 Photoluminescence of $BaZrO_3$ samples prepared for different pH

4. CONCLUSION

The sol-gel auto-combustion method was used to synthesize barium zirconate nanoparticles. The current synthesis technique produced high phase purity while being cost-effective. The XRD results illustrated a single cubic pure $BaZrO_3$ phase, and the pH 9 values are almost identical to the standard value. From FTIR, the gel showed significant vibration bands at 1445 cm^{-1} and other strong vibration bands at 849 cm^{-1}, which were attributed to the presence of pure $BaZrO_3$. SEM revealed that the particles were agglomerated. EDAX analysis verified that the synthesised materials had fully experienced the required chemical reactions to produce the needed perovskite-structured $BaZrO_3$ nanoparticles. From tauc plot, band gap of $BaZrO_3$ is decreases with increase in pH values. The emission spectrum of $BaZrO_3$ nanopowder for the three pH (5,7 &9), having strong green emission. The majority of lighting and display applications currently use inorganic phosphors, which convert a near-ultraviolet (n-UV) or blue LED chip emissions into a wide range of white light or specific colors for display applications.

Reference

[1] Robertson, J. (2000). Band offsets of wide-band-gap oxides and implications for future electronic devices. Journal of Vacuum Science & Technology B: Microelectronics and Nanometer Structures, *18(3), 1785*. doi:10.1116/1.591472

[2] Fabbri, E., Depifanio, A., Dibartolomeo, E., Licoccia, S., & Traversa, E. (2008). Tailoring the chemical stability of $Ba(Ce_{0.8-x}Zr_x)Y_{0.2}O_{3-\delta}$ protonic conductors for Intermediate Temperature Solid Oxide Fuel Cells (IT-SOFCs). Solid State Ionics, 179(15-16), 558–564. doi:10.1016/j.ssi.2008.04.002

[3] Azad, A.-M., Subramaniam, S., & Dung, T. W. (2002). On the development of high density barium metazirconate ($BaZrO_3$) ceramics. Journal of Alloys and Compounds, 334(1-2), 118–130. doi:10.1016/s0925-8388(01)01785-6

[4] Kochetova, N., Animitsa, I., Medvedev, D., Demin, A., & Tsiakaras, P. (2016). Recent activity in the development of proton-conducting oxides for high-temperature applications. RSC Advances, 6(77), 73222–73268. doi:10.1039/c6ra13347a

[5] Erb, A., Walker, E., & Flükiger, R. (1995). $BaZrO_3$: the solution for the crucible corrosion problem during the single crystal growth of high-Tc superconductors RE $Ba_2Cu_3O_{7-\delta}$; RE = Y, Pr. Physica C: Superconductivity, 245(3-4), 245–251. doi:10.1016/0921-4534(95)00123-9

[6] Yamanaka, S., Hamaguchi, T., Oyama, T., Matsuda, T., Kobayashi, S., & Kurosaki, K. (2003). Heat capacities and thermal conductivities of perovskite type $BaZrO_3$ and $BaCeO_3$. Journal of Alloys and Compounds, *359(1-2), 1–4*. doi:10.1016/s0925-8388(03)00137-3

[7] Kochetova, N., Animitsa, I., Medvedev, D., Demin, A., & Tsiakaras, P. (2016). Recent activity in the development of proton-conducting oxides for high-temperature applications. RSC Advances, 6(77), 73222–73268. doi:10.1039/c6ra13347a

[8] Viviani, M., Buscaglia, M. ., Buscaglia, V., Leoni, M., & Nanni, P. (2001). Barium perovskites as humidity sensing materials. Journal of the European Ceramic Society, 21(10-11), 1981–1984. doi:10.1016/s0955-2219(01)00155-8

[9] Saini, D. S., Tripathy, S., Kumar, A., Sharma, S. K., Ghosh, A., & Bhattacharya, D. (2017). Impedance and modulus spectroscopic analysis of single phase BaZrO3 ceramics for SOFC application. Ionics, 24(4), 1161–1171. doi:10.1007/s11581-017-2282-8

[10] Vassen, R., Cao, X., Tietz, F., Basu, D., & Stöver, D. (2004). Zirconates as New Materials for Thermal Barrier Coatings. Journal of the American Ceramic Society, 83(8), 2023–2028. doi:10.1111/j.1151-2916.2000.tb01506.x

[11] Liang, R., Bonn, D. A., & Hardy, W. N. (2012). Growth of YBCO single crystals by the self-flux technique. Philosophical Magazine, 92(19-21), 2563–2581. doi:10.1080/14786435.2012.669065

[12] Ricote, S., & Bonanos, N. (2010). Enhanced sintering and conductivity study of cobalt or nickel doped solid solution of barium cerate and zirconate. Solid State Ionics, 181(15-16), 694–700. doi:10.1016/j.ssi.2010.04.007

[13] Bozza, F., Bator, K., Kubiak, W. W., & Graule, T. (2016). Effects of Ni doping on the sintering and electrical properties of $BaZr_{0.8}Y_{0.2}O_{3-\delta}$ proton conducting electrolyte prepared by Flame Spray Synthesis. Journal of the European Ceramic Society,36(1),101107.

doi:10.1016/j.jeurceramsoc.2015.09.010

[14] Morishita, H., Ikebe, Y. and Ban, E. (2018) Proton Conductivity of Ni, Y Co-Doped BaZrO3. Journal of Materials Science and Chemical Engineering, 6, 19-27. doi:10.4236/msce.2018.66002

[15] Guillaume, B., Boschini, F., Garcia-Cano, I., Rulmont, A., Cloots, R., & Ausloos, M. (2005). Optimization of BaZrO3 sintering by control of the initial powder size distribution; a factorial design statistical analysis. Journal of the European Ceramic Society, 25(16), 3593–3604. doi:10.1016/j.jeurceramsoc.2004.09.022

[16] Munir, Z. A., & Anselmi-Tamburini, U. (1989). Self-propagating exothermic reactions: The synthesis of high-temperature materials by combustion. Materials Science Reports, 3(7-8), 277–365. doi:10.1016/0920-2307(89)90001-7

[17] A.S. Rogachev, A.S. Mukasyan, Combustion for Material Synthesis, CRC Press, New York, 2014. https://www.routledge.com/Combustion-for-Material-Synthesis/Rogachev-Mukasyan/p/book/9781482239515.

[18] Sutka, A., & Mezinskis, G. (2012). Sol-gel auto-combustion synthesis of spinel-type ferrite nanomaterials. Frontiers of Materials Science, *6*, 128-141.

[19] Tsay, J., & Fang, T. (2004). Effects of Molar Ratio of Citric Acid to Cations and of pH Value on the Formation and Thermal-Decomposition Behavior of Barium Titanium Citrate. Journal of the American Ceramic Society, 82(6), 1409–1415. doi:10.1111/j.1151-2916.1999.tb01931.x

[20] Kanie, K., Seino, Y., Matsubara, M., Nakaya, M., & Muramatsu, A. (2014). Hydrothermal synthesis of $BaZrO_3$ fine particles controlled in size and shape and fluorescence behavior by europium doping. New J. Chem., 38(8), 3548–3555. doi:10.1039/c4nj00443d

[21] Varma, A., Mukasyan, A. S., Rogachev, A. S., & Manukyan, K. V. (2016). Solution Combustion Synthesis of Nanoscale Materials. Chemical Reviews, 116(23), 14493–14586. doi:10.1021/acs.chemrev.6b00279

[22] Manju, P., Ajith, M. R., & Jaiswal-Nagar, D. (2019). Synthesis and characterization of $BaZrO_3$ nanoparticles by citrate-nitrate sol-gel auto-combustion technique: systematic study for the formation of dense $BaZrO_3$ ceramics. Journal of the European Ceramic Society. doi:10.1016/j.jeurceramsoc.2019.03.048

[23] Manju, P., Babu, A., SP, S., Tirumalarao, D., PV, A., Kamble, V. B., & Jaiswal-Nagar, D. (2022). Variation of citrate to metal cation ratio for dense and phase pure BaZrO3 via autocombustion synthesis. Journal of the American Ceramic Society, 105(8), 5082-5101.

[24] Yue, Z., Guo, W., Zhou, J., Gui, Z., & Li, L. (2004). Synthesis of nanocrystilline ferrites by sol–gel combustion process: the influence of pH value of solution. Journal of Magnetism and Magnetic Materials, 270(1-2), 216–223. doi:10.1016/j.jmmm.2003.08.025

[25] Chaturvedi, S., & Dave, P. N. (2013). Review on Thermal Decomposition of Ammonium Nitrate. Journal of Energetic Materials, 31(1), 1–26. doi:10.1080/07370652.2011.573523

[26] Liu, R. S., Wang, W. N., Chang, C. T., & Wu, P. T. (1989). Synthesis and characterization of high-Tc superconducting oxides by the modified citrate gel process. Japanese journal of applied physics, 28(12A), L2155.

[27] Aoki, A. (1990). Preparation of High-Quality Bi-Pb-Sr-Ca-Cu Oxide Precursor by the Citrate Gel Process. Japanese Journal of Applied Physics, 29(Part 2, No. 2), L270–L272. doi:10.1143/jjap.29.l270

[28] Devi, S. P., & Maiti, H. S. (1994). A modified citrate gel route for the synthesis of phase pure Bi2Sr2CaCu2O8 superconductor. Journal of Materials Research, 9(06), 1357–1362. doi:10.1557/jmr.1994.1357

[29] Roy, S., Sharma, D. A., Roy, S. N., & Maiti, H. S. (1993). Synthesis of YBa2Cu3O7−x powder by autoignition of citrate-nitrate gel. Journal of Materials Research, 8(11), 2761–2766. doi:10.1557/jmr.1993.2761

[30] Ostafiychuk, B. K., Kaykan, L. S., Kaykan, J. S., Deputat, B. Y., & Shevchuk, O. V. (2017). Composition, microstructure, and electrical properties control of the powders synthesized by sol–gel auto-combustion method using citric acid as the fuel. Nanoscale Research Letters, 12(1), 1-9.

[31] Danks, A. E., Hall, S. R., & Schnepp, Z. (2016). The evolution of “sol–gel” chemistry as a technique for materials synthesis. Materials Horizons, 3(2), 91–112. doi:10.1039/c5mh00260e

[32] Novitskaya, E., Kelly, J. P., Bhaduri, S., & Graeve, O. A. (2020). A review of solution combustion synthesis: an analysis of parameters controlling powder characteristics. International Materials Reviews, 1–27. doi:10.1080/09506608.2020.1765603

[33] Pavlović, V. P., Nikolić, M. V., Pavlović, V. B., LABUS, N., ŽIvkoviĆ, L., & StojanoviĆ, B. D. (2005). Correlation Between Densification Rate and Microstructure Evolution of Mechanically Activated BaTiO3. Ferroelectrics, 319(1),75– 85. doi: 10.1080/ 00150190590965451

[34] Brzezińska-Miecznik, J., Haberko, K., & Bucko, M. M. (2002). Barium zirconate ceramic powder synthesis by the coprecipitation–calcination technique. Materials Letters, 56(3), 273–278. doi:10.1016/s0167-577x(02)00454-8

[35] Veith, M., Mathur, S., Lecerf, N., Huch, V., Decker, T., Beck, H. P., Haberkorn, R. (2000). Journal of Sol-Gel Science and Technology, 17(2), 145–158. doi:10.1023/a:1008795419020

[36] Taglieri, G., Tersigni, M., Villa, P. ., & Mondelli, C. (1999). Synthesis by the citrate route and characterisation of BaZrO3, a high tech ceramic oxide: preliminary results. International Journal of Inorganic Materials, 1(1), 103–110. doi:10.1016/s1463-0176(99)00016-2

[37] Jubu, P. R., Yam, F. K., Igba, V. M., & Poay, B. K. (2020). Tauc-plot scale and extrapolation effect on bandgap estimation from UV–vis–NIR data – A case study of β-Ga2O3. Journal of Solid State Chemistry, 121576. doi:10.1016/j.jssc.2020.121576

[38] Ou, S.-L., Wuu, D.-S., Fu, Y.-C., Liu, S.-P., Horng, R.-H., Liu, L., & Feng, Z.-C. (2012). Growth and etching characteristics of gallium oxide thin films by pulsed laser deposition. Materials Chemistry and Physics, 133(2-3), 700–705. doi:10.1016/j.matchemphys.2012.01.060

[39] Sun, D., Li, D., Zhu, Z., Xiao, J., Tao, Z., & Liu, W. (2012). Photoluminescence properties of europium and titanium co-doped BaZrO3 phosphors powders synthesized by the solid-state reaction method. Optical Materials, 34(11), 1890–1896. doi:10.1016/j.optmat.2012.05.024

[40] Pankove, J. I. (1975). Optical processes in semiconductors. Courier Corporation.

[41] Ghobadi, N. (2013). Band gap determination using absorption spectrum fitting procedure. International Nano Letters, 3(1). doi:10.1186/2228-5326-3-2

[42] Wood, D. L., & Tauc, J. (1972). Weak Absorption Tails in Amorphous Semiconductors. Physical Review B, 5(8), 3144–3151. doi:10.1103/physrevb.5.3144

[43] Longo, V. M., de Figueiredo, A. T., de Lázaro, S., Gurgel, M. F., Costa, M. G. S., Paiva-Santos, C. O., Franco, R. W. A. (2008). doi:10.1063/1.2956741

[44] Montoncello, F., Carotta, M. C., Cavicchi, B., Ferroni, M., Giberti, A., Guidi, V., Meinardi, F. (2003). Near-infrared photoluminescence in titania: Evidence for phonon-replica effect. Journal of Applied Physics, 94(3), 1501–1505. doi:10.1063/1.1586961

[45] Longo, V. M., Cavalcante, L. S., de Figueiredo, A. T., Santos, L. P. S., Longo, E., Varela, J. A., … Hernandes, A. C. (2007). Highly intense violet-blue light emission at room temperature in structurally disordered SrZrO3 powders. Applied Physics Letters, 90(9), 091906. doi:10.1063/1.2709992

[46] Cavalcante, L. S., Sczancoski, J. C., De Vicente, F. S., Frabbro, M. T., Li, M. S., Varela, J. A., & Longo, E. (2008). Microstructure,

dielectric properties and optical band gap control on the photoluminescence behavior of Ba[Zr0.25Ti0.75]O3 thin films. Journal of Sol-Gel Science and Technology, 49(1), 35–46. doi:10.1007/s10971-008-1841-x

[47] Hirayama, H., Maeda, N., Fujikawa, S., Toyoda, S., & Kamata, N. (2014). Recent progress and future prospects of AlGaN-based high-efficiency deep-ultraviolet light-emitting diodes. Japanese Journal of Applied Physics, 53(10), 100209. doi:10.7567/jjap.53.100209

[48] Shen, K.-C., Ku, C.-T., Hsieh, C., Kuo, H.-C., Cheng, Y.-J., & Tsai, D. P. (2018). Deep-Ultraviolet Hyperbolic Metacavity Laser. Advanced Materials, 30(21), 1706918. doi:10.1002/adma.201706918

[49] Rong, X., Wang, X., Ivanov, S. V., Jiang, X., Chen, G., Wang, P., Shen, B. (2016). High-Output-Power Ultraviolet Light Source from Quasi-2D GaN Quantum Structure. Advanced Materials, 28(36), 7978–7983. doi:10.1002/adma.201600990

[50] Le, B. H., Zhao, S., Liu, X., Woo, S. Y., Botton, G. A., & Mi, Z. (2016). Controlled Coalescence of AlGaN Nanowire Arrays: An Architecture for Nearly Dislocation-Free Planar Ultraviolet Photonic Device Applications. Advanced Materials, 28(38), 8446–8454. doi:10.1002/adma.201602645

[51] Chichibu, S. F., Kojima, K., Uedono, A., & Sato, Y. (2016). Defect-Resistant Radiative Performance ofm-Plane Immiscible Al1−xInxN Epitaxial Nanostructures for Deep-Ultraviolet and Visible Polarized Light Emitters. Advanced Materials, 29(5), 1603644. doi:10.1002/adma.201603644

[52] Li, D., Jiang, K., Sun, X., & Guo, C. (2018). AlGaN photonics: recent advances in materials and ultraviolet devices. Advances in Optics and Photonics, 10(1), 43. doi:10.1364/aop.10.000043

[53] AlQatari, F., Sajjad, M., Lin, R., Li, K. H., Schwingenschlogl, U., & Li, X. (2018). Optical properties of BalN and BGaN for applications in latticematched UV optical structures. arXiv preprint arXiv:1803.10011.